

This is the accepted manuscript made available via CHORUS. The article has been published as:

Bimodal entanglement entropy distribution in the many-body localization transition

Xiongjie Yu, David J. Luitz, and Bryan K. Clark

Phys. Rev. B **94**, 184202 — Published 15 November 2016

DOI: [10.1103/PhysRevB.94.184202](https://doi.org/10.1103/PhysRevB.94.184202)

Bimodal entanglement entropy distribution in the many-body localization transition

Xiongjie Yu,¹ David J. Luitz,¹ and Bryan K. Clark¹

¹*Institute for Condensed Matter Theory and Department of Physics,
University of Illinois at Urbana-Champaign, Urbana, IL 61801, USA*

We introduce the cut averaged entanglement entropy in disordered periodic spin chains and prove it to be a concave function of subsystem size for individual eigenstates. This allows us to identify the entanglement scaling as a function of subsystem size for individual states in inhomogeneous systems. Using this quantity, we probe the critical region between the many-body localized (MBL) and ergodic phases in finite systems. In the middle of the spectrum, we show evidence for bimodality of the entanglement distribution in the MBL critical region, finding both volume law and area law eigenstates over disorder realizations as well as within *single disorder realizations*. The disorder averaged entanglement entropy in this region then scales as a volume law with a coefficient below its thermal value. We discover in the critical region, as we approach the thermodynamic limit, that the cut averaged entanglement entropy density falls on a one-parameter family of curves. Finally, we also show that without averaging over cuts the slope of the entanglement entropy *vs.* subsystem size can be negative at intermediate and strong disorder, caused by rare localized regions in the system.

PACS numbers: 75.10.Pq, 03.65.Ud, 71.30.+h

I. INTRODUCTION

The many body localization (MBL) transition is a dynamical phase transition driven by the interplay of strong interactions and disorder^{1,2}. While disordered noninteracting systems in one dimension localize for arbitrarily small disorder³, the presence of interactions thermalizes quantum systems up to a finite critical disorder strength. This thermalization is typically expected to occur through the eigenstate thermalization hypothesis⁴⁻⁷ (ETH), which states that local few-body observables become a smooth function of the energy. Furthermore, their canonical expectation values match those obtained from the mixed state thermal density matrix at inverse temperature β , chosen such that the thermal expectation value of the energy $\langle H \rangle_\beta = \frac{1}{Z} \text{Tr}(e^{-\beta H} H)$ is equal to the eigenenergy of the state. To satisfy this, the reduced density matrix of individual eigenstates at energy E becomes equal to the thermal density matrix, leading to an extensive (volume law) entanglement entropy.

On the other hand, in the MBL phase at stronger disorder the ETH is no longer valid. While ETH is a consequence of quantum chaos (a generic feature of interacting nonintegrable systems⁸), the MBL phase shows features of integrability, most prominently signaled in a change of the spectral statistics that was explored in several pioneering works⁹⁻¹¹ and are now a standard measure for the detection of MBL¹²⁻¹⁶. The integrability in the MBL phase is due to an emergent extensive number of local conserved quantum operators¹⁷⁻¹⁹, which prohibit thermalization and lead to a subextensive (area law) entanglement entropy; this has been numerically verified in many studies^{14,20-24}. In particular, after the transition to the full MBL regime, nearly all eigenstates exhibit area law entanglement^{20,22-24} at arbitrarily high energies.

While the ETH is typically only expected²⁵ to be valid for subsystems of size ℓ such that $\ell/L \rightarrow 0$, evidence for

the MBL transition typically considers the average half-cut entanglement entropy averaged over the ensemble of disorder realizations, finding it to either follow a volume law (in the ergodic region) or an area law (in the MBL region). In this work, we will consider subsystem sizes which are a constant fraction ($< \frac{1}{2}$) of the entire system.

Although the many-body localized and ergodic phases have been heavily studied, the transition between them is still subject to debate. On general grounds, it has been argued that the scaling of the entanglement entropy at the critical point should follow a volume law²⁶, whereas phenomenological RG calculations point to a strongly fluctuating behavior²⁷. Other studies point to strong multifractal behavior at the critical point^{28,29} and the possibility of a power law scaling of the entanglement entropy as $S \propto L^\alpha$ with an exponent $\alpha < 1$ (*i.e.* slower than volume law)³⁰.

In this work, we consider the properties of the transition (as well as the adjoining phases), by focusing on the *cut-averaged entanglement entropy* (CAEE) $\tilde{S}(\ell)$ (as in Eq. (CAEE)) and its slope (SCAEE) (as in Eq. (SCAEE)) of subsystems with size ℓ at a fixed ratio of ℓ/L . Cut averaging here literally means averaging over all subsystems of a particular size ℓ . The CAEE for any eigenstate of a periodic system is a concave function of ℓ (*cf.* lower panel of Fig. 1 as opposed to the upper panel for the entropy without cut average). We prove this using strong subadditivity (SSA) in Sec. II. The CAEE and SCAEE can be used to directly identify the volume or area law scaling in single eigenstates.

Using these concepts, we study the distribution of the SCAEE over disorder realizations. This distribution appears Gaussian at weak disorder, while at moderate disorder in the ergodic region the distribution is generically non-Gaussian for system sizes we can access, a feature that has been observed also in the distributions of the diagonal²¹ and off-diagonal³¹ matrix elements of local

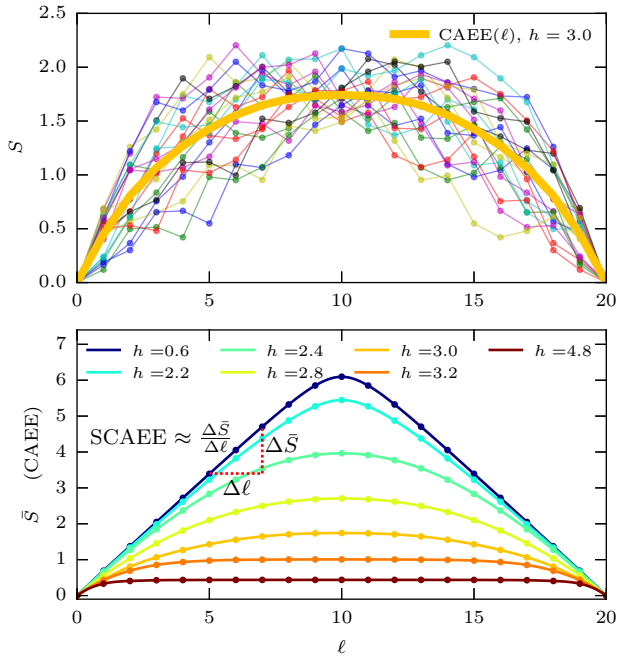


Figure 1. **Top:** von Neumann entanglement entropies (S) for different fixed left cut positions as a function of subsystem size ℓ of a single eigenstate for one sample with system size $L = 20$ and disorder strength $h = 3.0$. Notice that the $S(\ell)$ curves are in general not differentiable. However, the cut-averaged entanglement entropy (CAEE, defined in Eq. (CAEE)) is a smooth and concave function of ℓ . **Bottom:** Typical CAEE (denoted as $\bar{S}(\ell)$) sampled from different disorder strengths, for periodic Heisenberg chains of length $L = 20$. Each curve is generated from a single eigenstate of *one* disorder realization. The slope of CAEE, abbreviated as SCAEE and defined in Eq. (SCAEE), can directly probe the volume law or area law scaling behavior of an eigenstate.

operators in the eigenbasis of the Hamiltonian. On the MBL side, the distribution of the SCAEE is peaked at zero slope and has an exponential tail. In addition, in the MBL and ergodic phases the variance of this distribution gets smaller as a function of system size L , which naturally suggests that the variance approaches zero in the thermodynamic limit (TDL); this would leave all eigenstates to follow either an area law (SCAEE equal to 0) or a volume law (SCAEE close to $\ln(2)$).

In the transition region, we also find that as the system size grows, \bar{S}/L at a fixed subsystem ratio of ℓ/L appears to approach a one-parameter family of curves, which can be parameterized by the value of the CAEE or the SCAEE at any ℓ/L .

Most interestingly, in the critical regime we find that the distribution of the SCAEE is bimodal both over multiple disorder realizations as well as for *single disorder realizations*. The variance of the SCAEE distribution in the transition region seems to grow with system size when considered over disorder realizations. Our system sizes are too small to pin down its maximal value, but they

are consistent with (among other possibilities) the maximal variance possible which would lead to half the states having zero SCAEE and half having maximal SCAEE. This scenario would lead to an entanglement entropy at the transition which scales as a volume law with half its thermal value.

II. STRONG SUBADDITIVITY AND ENTANGLEMENT ENTROPY UNDER PERIODIC BOUNDARY CONDITIONS

Strong subadditivity (SSA) is a theorem of entropy, applicable to both classical and quantum entropies³². SSA of the von Neumann entropy was proved by E.H. Lieb and M.B. Ruskai in 1973³³, and can be formulated as many equivalent inequalities^{33–36}. The von Neumann entanglement entropy $S(A)$ quantifies the entanglement of subsystem A with the rest of the system and is obtained from the reduced density matrix, given by a partial trace of the degrees of freedom in the *complement* of subsystem A :

$$S = -\text{Tr}_A (\text{Tr}_B |\psi\rangle\langle\psi|) \ln (\text{Tr}_B |\psi\rangle\langle\psi|). \quad (1)$$

As recently pointed out by Tarun Grover²⁶, for MBL systems, SSA ensures that the disorder averaged von Neumann entanglement entropy at any energy density is concave, where $\bar{S}(\ell, e)$ is averaged over a tiny energy density window and all disorder configurations.

Unfortunately, without disorder averaging, the curve $S(\ell)$ for individual eigenstates obeys no concavity conditions showing essentially random behavior, which stems from the local entanglement structure (*cf.* Fig. 1 Top).

In this section, we show how to use SSA to derive constraints on $S(\ell)$ in the continuum for any *individual state* in a periodic one-dimensional system where the von Neumann entanglement entropy is averaged over all cuts with subsystem size ℓ . The lattice version of the derivation is available in Appendix A. This average over all subsystems of size ℓ is sufficient to restore concavity for individual states (see Eq. (CAEE)) and puts constraints on the sign of the slope at different ℓ (see Eq. (SCAEE)). This can be used to identify whether individual states separately obey an ‘area law’ or a ‘volume law’. We note that the result in Ref. 26 for periodic systems is a direct corollary of this result as the sum of concave functions is concave.

For the following, x denotes the center position of a simply connected subsystem. We define the cut-averaged entanglement entropy (CAEE) as

$$\bar{S}(\ell) \equiv \frac{1}{L} \int_0^L dx S(x, \ell), \quad (\text{CAEE})$$

and define the slope of the cut-averaged entanglement

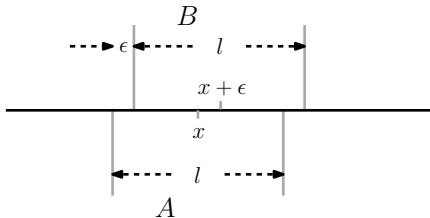


Figure 2. A typical arrangement of the subsystems to apply the strong subadditivity (SSA) inequality $S(A) + S(B) \geq S(A \cup B) + S(A \cap B)$. A continuous subsystem can be characterized sufficiently by its length ℓ and the position of its middle point x in 1D.

entropy (SCAEE) as

$$\frac{\partial \bar{S}}{\partial \ell} \equiv \frac{1}{L} \frac{\partial}{\partial \ell} \int_0^L dx S(x, \ell). \quad (\text{SCAEE})$$

For a density matrix of any quantum state, according to SSA, the von Neumann entanglement entropy obeys

$$S(A) + S(B) \geq S(A \cup B) + S(A \cap B). \quad (2)$$

We apply this where A and B are subsystems of equal length, but slightly shifted apart as in Fig. 2. Translational invariance is not assumed due to the presence of disorder and we focus on single eigenstates of a particular disorder pattern from now on.

The inequality (2) is equivalent to

$$S(x, \ell) + S(x + \epsilon, \ell) \geq S(x + \frac{\epsilon}{2}, \ell + \epsilon) + S(x + \frac{\epsilon}{2}, \ell - \epsilon). \quad (3)$$

When expanded to second order in ϵ , it becomes

$$\frac{\partial^2 S(x, \ell)}{\partial^2 \ell} \leq \frac{1}{4} \frac{\partial^2 S(x, \ell)}{\partial^2 x}. \quad (4)$$

For a system with periodic boundary conditions, by integrating the above equation over the entire system, it is easy to see that

$$\frac{\partial^2}{\partial^2 \ell} \bar{S}(\ell) \leq 0, \quad (5)$$

because the boundary terms at $x = 0$ and $x = L$ cancel each other exactly. Eq. (5) puts a constraint on the concavity of $\bar{S}(\ell)$ which holds for any given eigenstate of an arbitrary disorder configuration, because SSA is applicable to the density matrix of any quantum state.

There exists an essentially equivalent constraint on the first derivative of $\bar{S}(\ell)$, based on an equivalent formulation of the SSA theorem as in Fig. 3.

$$S(A \cup B) + S(B \cup C) \geq S(A) + S(C), \quad (6)$$

When written explicitly, it becomes

$$S(x + \frac{\epsilon}{2}, \ell + \epsilon) + S(x + \ell + \frac{\epsilon}{2}, \ell + \epsilon) \geq S(x, \ell) + S(x + \ell + \epsilon, \ell). \quad (7)$$

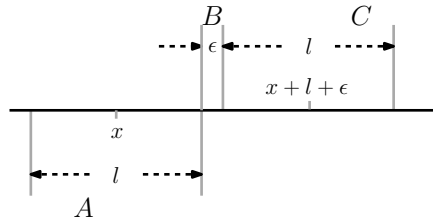


Figure 3. A typical arrangement of the subsystems to apply the strong subadditivity (SSA) inequality $S(A \cup B) + S(B \cup C) \geq S(A) + S(C)$. A and C are non-overlapping, which means $l < L/2$, where L is the length of the entire periodic system.

One can expand it to the first order in ϵ

$$\frac{\partial S(x, \ell)}{\partial \ell} + \frac{\partial S(x + \ell, \ell)}{\partial \ell} \geq \frac{1}{2} \frac{\partial S(x + \ell, \ell)}{\partial x} - \frac{1}{2} \frac{\partial S(x, \ell)}{\partial x}. \quad (8)$$

Again, with periodic boundary conditions, integrating the above equation over the entire system reduces to

$$\frac{\partial \bar{S}(\ell)}{\partial \ell} \geq 0. \quad (9)$$

where $\ell < L/2$.

The lattice version of the derivation can be found in Appendix A. The two constraints (5) and (9) imply that the cut averaged entanglement entropy $\bar{S}(\ell)$ is a concave function of subsystem size with positive slope for $0 \leq \ell \leq L/2$ and negative slope for $L/2 \leq \ell \leq L$. Its negative second derivative makes the slope of larger subsystems at most equal to or smaller than the slope of smaller subsystems. It should be emphasized that these considerations are only valid for the cut averaged entanglement entropy in periodic systems. Without this average, the ‘slope’ of the $S(\ell)$ curve can become negative even for $\ell < L/2$, which we argue to be a sign for localized regions in the system (cf. Fig. 8).

III. MODEL AND METHOD

We study the “standard model” of the MBL transition: The periodic random field Heisenberg chain^{12–14,21–24,37–45}, described by the Hamiltonian

$$H = \sum_{i=1}^L \hat{S}_i \cdot \hat{S}_{i+1} + h_i \hat{S}_i^z, \quad h_i \in [-h, h]; \quad p(h_i) = \frac{1}{2h}, \quad (10)$$

where the site dependent magnetic field h_i is a uniform random number, coupling to \hat{S}_i^z . In this system current evidence primarily suggests an MBL transition which occurs at a critical disorder strength $h_c \approx 3.7$ in the center of the spectrum^{13,14}, although the value of h_c is not fully settled⁴⁶.

Interior eigenpairs are obtained using a shift-invert technique, where the Hamiltonian is transformed to

$(\mathbf{H} - \sigma)^{-1}$, with a target energy σ inside the spectrum. The transformed problem is then amenable to standard Krylov space methods to obtain eigenpairs from the (upper and lower) edges of the transformed spectrum, reducing the computational difficulty virtually to the problem of applying the inverse of the shifted Hamiltonian to arbitrary vectors. This is a formidable task, due to the rapid growth of the problem dimension and high density of states in the middle of the spectrum. Currently, no more than $L = 22$ spins in the $S_z = 0$ sector of the random Heisenberg chain can be treated using the shift-invert methodology even when applied in a massively parallel way¹⁴. Throughout this work, we address eigenpairs in the center of the spectrum at fixed energy density $\epsilon = (E - E_{\min})/(E_{\max} - E_{\min}) = 0.5$, where the extensive target energy E in each disorder configuration is determined by the corresponding groundstate (E_{\min}) and antigrandstate (E_{\max}) energies.

IV. CUT AVERAGED ENTANGLEMENT ENTROPY (CAEE)

The considerations in Sec. II (and appendix A) represent a strong constraint on the CAEE as a function of subsystem size. In particular, for $\ell \leq L/2$, the CAEE for larger subsystems always has to be larger than (or equal to) the ones for smaller subsystems. Note that, while this property holds for individual disorder realizations, the disorder average of the cut-averaged entanglement entropy is identical with the disorder average of the standard (single cut) entanglement entropy.

The bottom panel of Figure 1 shows typical CAEE curves as a function of subsystem size ℓ obtained from single (mid-spectrum) eigenstates of the Hamiltonian at various disorder strengths h . Due to the subadditivity constraints, the value of the CAEE at a given subsystem size has to be correlated with its values at other subsystem sizes. The CAEE curve is mirror symmetric around $\ell = L/2$ and finite size effects seem to be strongest in the region of the half cut, especially for the slope of the curve. We therefore primarily focus on the quarter cut $\ell = L/4$, where these effects are much less important. Notice that in the absence of cut averaging (*cf.* top panel of Figure 1), the entanglement entropy as a function of subsystem size is non-differentiable and therefore its slope is not well defined.

For each eigenstate, we calculate the reduced density matrix of all possible cuts of the system with a fixed subsystem length ℓ and average the von Neumann entropy over them. This is repeated for all subsystem sizes $\ell \in [1, L/2]$, yielding the CAEE $\bar{S}(\ell)$ as a function of the (integer) subsystem size ℓ . In the next step, we interpolate this set of points (extended down to $\ell = 0$ and up to $\ell = L$ by the symmetry $S_\ell = S_{L-\ell}$) by a cubic spline, yielding a smooth and continuous function of $\bar{S}(\ell)$. The result for several typical states is depicted by the lines connecting the points of Fig. 1 for various values of the

disorder strength. This allows us to look at derivatives of the entanglement entropy curve at fixed ratio ℓ/L , which ensures the limit of an extensive subsystem size and can be estimated even for system sizes, where ℓ/L is incommensurate with the lattice. We have checked that using discrete derivatives (for the commensurate cases) yields virtually identical results and does not change the conclusions of this work. The corresponding derivation of the bounds in the discrete case is provided in appendix A.

A. Cut averaged entanglement entropy slope (SCAEE)

We calculate the CAEE $\bar{S}(\ell)$ as a function of subsystem size for all eigenstates at fixed energy density $\epsilon = 0.5$ and determine the SCAEE $\partial\bar{S}(\ell)/\partial\ell$. A fully ergodic eigenstate should have a SCAEE close to its maximal value: $\ln 2$. On the other hand, if the state is fully localized, the slope should be close to zero. In this section, we present detailed results on the SCAEE in different regimes; we consider its distribution over disorder realizations considering the first and second moment of the distribution as well as the entire distribution itself.

1. Mean slope

We begin with the mean of the SCAEE for subsystems of size $\ell = L/4$ for different system sizes. The top panel of Fig. 4 shows the result obtained from the disorder average over $\approx 10^3$ disorder configurations and ≈ 50 eigenstates per realization as a function of disorder strength. The best estimate of the critical point in the center of the spectrum from Ref. 14 is indicated by the vertical dashed line.

At weak disorder, the slope gets closer to its maximal value of $\ln 2$ for increasing system size. In addition, at larger system sizes, the $\ln 2$ plateau extends to larger values of h consistent with the idea of a sharp transition away from $\ln 2$ in the TDL. Near the critical point, the average slope decreases rapidly to a smaller (near zero) value in the MBL phase. As the system size grows, the slope outside the critical region decreases as system size increases. These behaviors are fully consistent with the results obtained for other quantities and in particular the entanglement entropy density S/L , studied in Ref. 14, a quantity that is closely related to the SCAEE if averaged over disorder, as we shall see in Sec. IV B.

In the critical region we see that the mean SCAEE for different system sizes generally intersect. While finite size effects will cause this crossing to drift with system size, we may treat it as a rough estimate for the critical point and find it consistent with the critical h_c estimated by other approaches^{13,14}.

It is interesting to note that the mean SCAEE is approximately 0.1 at this crossing point. Again, noting

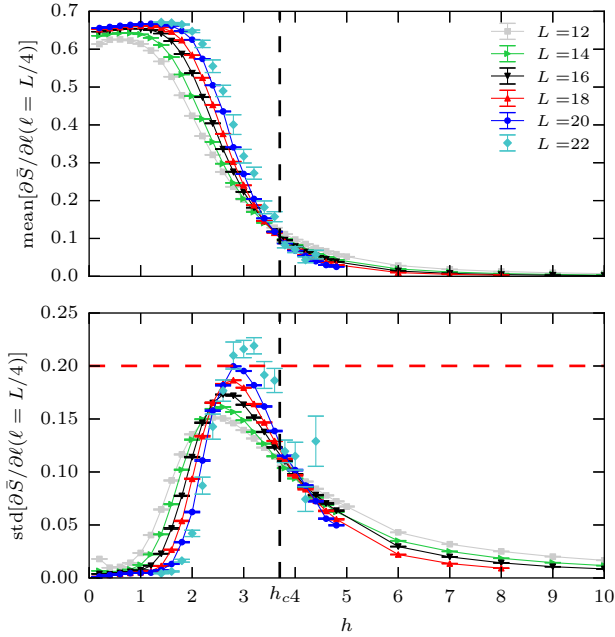


Figure 4. Disorder averaged mean entanglement entropy slope (top) and standard deviation of the mean entanglement entropy slope (bottom). The black dashed lines mark the rough intersecting positions of the curves of different system sizes. The red horizontal line for the bottom panel indicates the standard deviation of a uniform (box) distribution on the interval $[0, \ln 2]$, given by $\sigma_{\square} = \frac{\ln 2}{2\sqrt{3}}$. Note that the maximal variance of a bounded distribution on $[0, \ln 2]$ is given by a bimodal delta distribution, yielding $\sigma_{\text{max}} = \frac{\ln 2}{2} \approx .34657$. The maximum can at most saturate at this value.

that there will be a drift of this value, a non-zero slope implies a non-area law value of the entanglement at the transition.

2. Variance peak of the entanglement entropy slope

Recently, it has been discovered that the variance of the distribution of the entanglement entropy in MBL systems exhibits a maximum close to the MBL transition^{14,47,48}. In Fig. 4, we present results on the standard deviation of the SCAEE, $\text{std}[\partial \bar{S} / \partial \ell]$, for subsystem sizes $\ell = L/4$. This quantity also exhibits a maximum close to the transition and although the slope is an intensive quantity, the variance peak seems to grow in amplitude for the accessible system sizes $L \leq 22$.

Because the cut-averaged entanglement entropy slope is strictly bounded by $0 \leq \partial \bar{S} / \partial \ell \leq \ln 2$, the peak of the standard deviation can not grow infinitely and can at most saturate⁴⁹ at the maximal standard deviation given by a bimodal delta distribution $p(x) = \frac{1}{2} (\delta(x) + \delta(x - \ln 2))$.

We will discuss the origin of the variance peak of the entanglement entropy slope below, when we present the

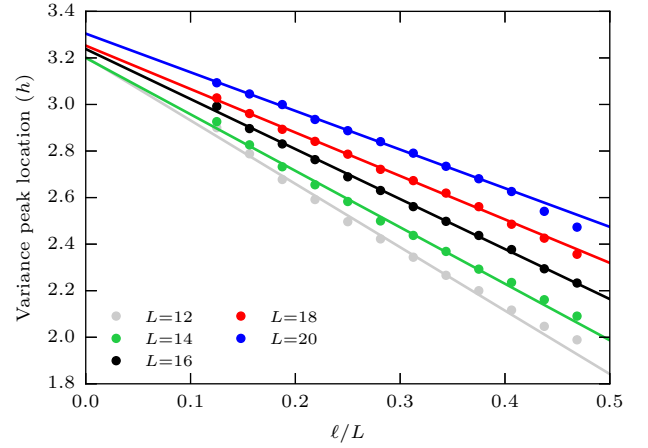


Figure 5. Variance peak locations at different subsystem ratio ℓ/L for various system sizes. The variance peak locations are extracted from standard deviation plots as in Fig. 4, where the discrete $\bar{S}(\ell)$ are interpolated by cubic splines. The solid lines are linear fit curves to data points. The variance peak location (h) rises with increasing system sizes. It is important to notice that for a particular L , the differences between the peak locations at different ratios becomes smaller, as L increases, which is reflected by the decreasing slope of the lines connecting different subsystem sizes.

full probability distributions of this quantity and show that it becomes bimodal close to the transition. This is clear from the behavior of the standard deviation with system size in Fig. 4, which grows for the available size as a function of L and exceeds the value obtained for a box distribution for system sizes larger or equal than $L = 20$. This bound is important as it represents the *largest* standard deviation of a unimodal distribution on $[0, \ln 2]$. Larger variances necessarily imply that the distribution has to be *multimodal* and the inspection of our histograms in Sec. IV A 3 clearly points to a bimodal distribution with maxima close to 0 and $\ln 2$.

We attempted polynomial extrapolations of the maxima of the variance to the TDL. Given our system sizes and the lack of justification for the scaling ansatz, such an extrapolation is obviously unreliable but the results are not inconsistent with the maxima reaching the maximal possible variance ($\frac{\ln 2}{2}$) close to the critical point ($h_c = 3.7(1)$).

In Fig. 4 we have chosen a subsystem of size $\ell = L/4$ to mitigate strong finite size effects occurring at the half cut. The difference between the peak locations of various subsystem ratios becomes smaller as system size grows (*cf.* Fig. 5). This suggests that the transition, as identified by the variance peak, occurs at the same value of h for all subsystem sizes in the TDL. This latter fact is a necessary condition if all states in the TDL have linear (possibly zero) SCAEE for all subsystem sizes.

3. Slope histogram

It is known from many studies^{21,27,42,50–54} that the surrounding of the MBL transition is dominated by rare region effects, responsible for subdiffusion^{42,51–53} on the thermal side of the transition. This is reflected in pathological (non-Gaussian) features of the probability distributions over disorder of various observables²¹. In particular the entanglement entropy^{20,21,24} develops long tails down to zero entanglement, although the mean remains extensive and the weight of the tails is exponentially suppressed.

Here, we are interested in the SCAEE, which can be expected to wash out some of the rare region effects, while capturing the dominant scaling behavior of the entanglement entropy. As in the above discussion, we focus on extensive subsystems, where we expect that the localization length ξ will be overcome at subsystem system sizes where $\ell \gg \xi$, thus providing a clear separation of dominant localized and delocalized behaviors for large system sizes.

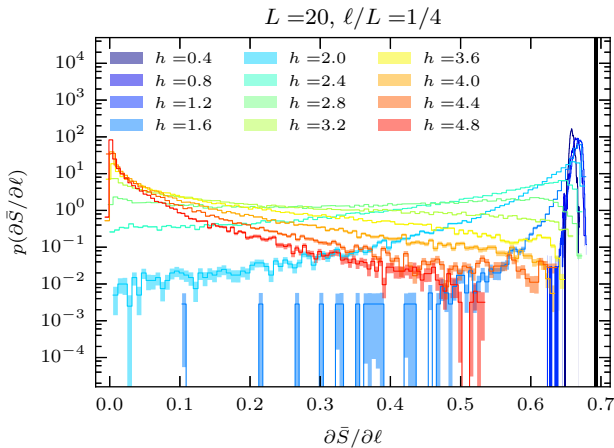


Figure 6. Probability distribution of SCAEE evaluated at $\ell = L/4$, for systems of size $L = 20$ at various disorder strengths. The black vertical line indicates the maximal slope of $\ln 2$.

At weak disorder, the distribution of the SCAEE shown in Fig. 6 is close to a normal distribution with a mean close to the maximal slope at $\ln 2$, indicated by the vertical line. As also seen in the entanglement entropy presented in Ref. 21, there may be small deviations from the normal distribution, surviving in the thermodynamic limit but significant tails start to develop only at slightly larger disorder strengths around $h \gtrsim 0.8$. The weight in the tails reduces with system size as seen in Fig. 7 but the distributions remain generically non-Gaussian starting at relatively small disorder strengths of $h \approx 1$.

Near the critical point (middle panels of Fig. 7), the distribution becomes broad, giving rise to the maximal variance as discussed in the previous section. In fact, with growing system sizes, the distribution becomes

increasingly bimodal, developing maxima close to zero (minimal) slope and $\ln 2$ (maximal) slope. As the position of the variance peak (lower panel of Fig. 1) moves towards the critical point for large systems and becomes sharp, we expect a bimodal distribution of the entanglement slope to be characteristic for the MBL transition. We show in Fig. 1 that the value of the variance at its maximum is already slightly larger than the value of a uniform distribution for systems of size $L = 20$ and is definitely larger than the uniform variance for larger system sizes (with growing tendency of the peak height for larger system sizes, possibly up to saturation at the theoretical maximum of the standard deviation at $\sigma_{\max} = \frac{\ln 2}{2\sqrt{3}}$). This rules out the possibility of a flat or unimodal distribution, leaving as the only possibility consistent with our results for the shapes of the distribution a bimodal distribution with maxima close to the minimal and maximal slope. Whether the weight between these maxima vanishes completely in the thermodynamic limit can not be definitely answered from our finite size results but this scenario is consistent with our data.

In the MBL phase, the maximum of the distribution of the SCAEE has clearly shifted towards very small slopes with an exponentially suppressed tail, extending up to the maximal slope. For the $h = 8.0$ plot, one observes a small weight for negative slopes, which are an artifact of our spline interpolation: For very low entanglement entropies, the spline tends to become oscillatory and leads to slightly negative slopes. This is not a problem for larger entanglement entropies.

While the SCAEE captures the *dominant* scaling behavior of the entanglement entropy, it has a tendency to hide the effect of rare (localized and ergodic) regions. Therefore, we also study the distribution of the discrete entanglement entropy slope $\Delta^- S(L/4) = S(L/4) - S(L/4 - 1)$ without averaging over cuts in Fig. 8. The most striking difference to the cut averaged slope is the absence of the SSA constraints, allowing for a *decrease* of the entanglement entropy with increasing system size, which can typically be expected if the boundary of the subsystem touches a localized part of the system as recently discussed in Ref. 21.

At weak disorder strength ($h \lesssim 0.8$), the histogram of $\Delta^- S$ approaches a Gaussian distribution for large system sizes, very similar to the cut averaged slope and no negative discrete slopes $\Delta^- S$ are observed. This changes significantly at intermediate disorder $h \gtrsim 2$, where more weight at negative discrete slopes is built up and a peak at 0 appears. We may speculate that this peak is caused by situations in which the changing subsystem boundary of the subsystems of length $L/4$ and $L/4 - 1$ both lie in a localized region, thus leading to a small change of the entanglement entropy and consequently $\Delta^- S = 0$. This peak becomes dominant in the MBL phase at $h \gtrsim 3.7$, where the distribution of $\Delta^- S$ becomes increasingly symmetric for larger system sizes with positive and negative discrete slopes being equally probable. The behaviour of these distributions is in very good agreement with the

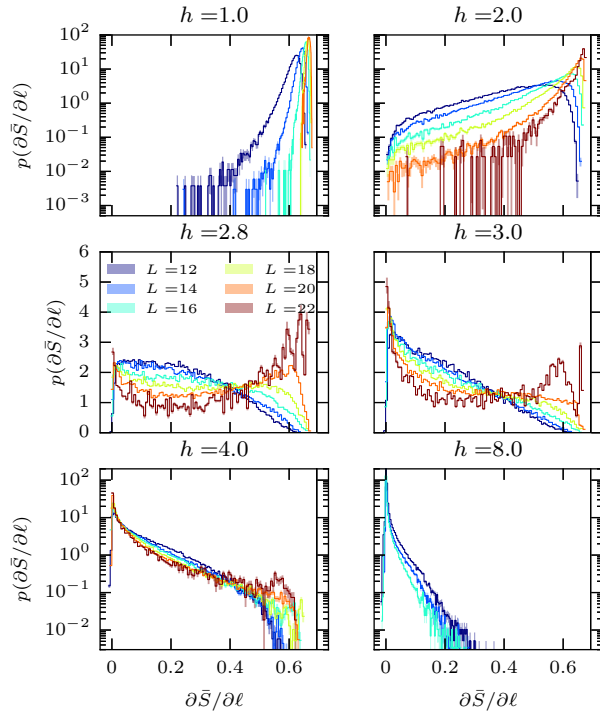


Figure 7. System size dependence of the probability distributions of SCAEE evaluated at $\ell/L = 1/4$. At weak disorder ($h = 1$ and $h = 2$), the distribution approaches a Gaussian distribution for large system sizes. For our finite systems, the zone showing critical behaviour is roughly at $h = 3.0$ and drifts to larger disorder strength for larger systems. We observe a clear signature of an emerging bimodal distribution. In the MBL phase ($h = 4$ and $h = 8$), the distribution is again unimodal and sharply peaked at zero slope. The black vertical line indicates the maximal slope of $\ln 2$. Note that the panels in the critical region are shown on a linear scale for clarity, while the other panels are on a logarithmic scale to exhibit the tails.

picture that rare localized regions of the system exist in the ergodic phase, while in the MBL phase the role of localized and delocalized regions switches and the latter become rare.

4. Variance peak of the entanglement entropy slope of individual disorder realizations

In Sec. IV A 3 we find a bimodal distribution of the SCAEE when sampled over eigenstates and disorder realizations. Here, we consider this distribution over single disorder realizations. In particular, we show that (i) eigenstates within a single sample can (but do not always) show bimodal behavior of the SCAEE (ii) partially contribute to the variance of the SCAEE seen in Sec. IV A 2 and (iii) have values of the SCAEE which are not independent of each other. This means that within *one disorder realization* some eigenstates show area law scal-

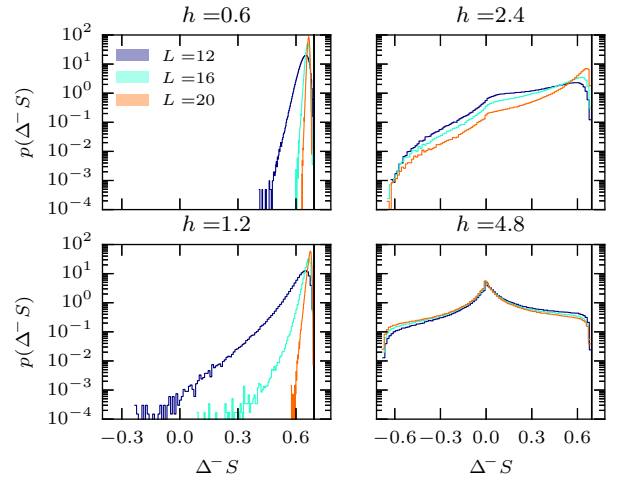


Figure 8. Discrete entanglement entropy “slope” $\Delta^-S(L/4) = S(L/4) - S(L/4 - 1)$ of the raw entanglement entropy *without averaging over all subsystem cuts*. The appearance of negative slopes is associated with localized regions²¹.

ing of the entanglement entropy, while others scale by a volume law, at fixed *energy density*.

There are two extreme limits that can be considered in understanding the variance of the SCAEE. In one case, each disorder realization could individually contain eigenstates that all have (near) maximal or (near) zero SCAEE and hence individually have (near) zero variance. Then the entire variance results from a distribution over different disorder realizations. Alternatively, every eigenstate in a given disorder realization could be uncorrelated with each other. We can emulate this case by independently sampling states from the middle panels of fig. 7. Sampling groups of 50 eigenstates at $L = 20$ and $h = 2.8$ we see that the standard deviation of each group of 50 samples is a tight Gaussian centered around 0.2. We find our data is consistent with neither extreme. Instead, both effects seem to be relevant for the overall variance in Fig. 4.

In order to understand if the large variance of the entanglement entropy and its slope can also be (partly) created by single disorder realizations, we calculate the standard deviation of the SCAEE *for single disorder realizations* at fixed energy density $\epsilon = 0.5$ from approximately 50 eigenstates per disorder configuration. Fig. 9 shows a two dimensional histogram of the per-sample standard deviation of the SCAEE $\text{std}[\partial\bar{S}(L/4)/\partial\ell]$ for different disorder strengths and system sizes $L = 12$ and $L = 20$. Most disorder realizations show a larger variance of the SCAEE close to the critical point at $L = 12$ and the disorder averaged standard deviation (mean of the histogram) shown by the black line looks very similar to the overall variance peak shown in Fig. 4. For larger systems, we see the following two trends in the critical regime (*cf.* Fig. 10 for a cut through Fig. 9 in the critical regime). First, the distributions over a single sample

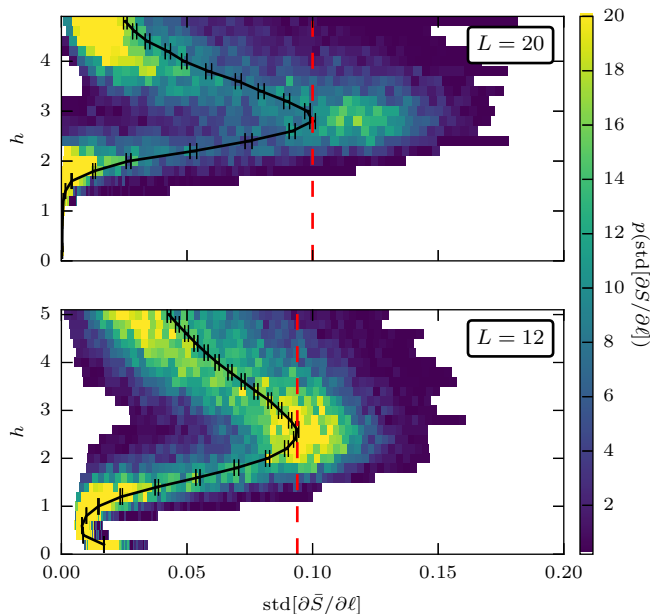


Figure 9. Probability density of the standard deviation of the SCAEE $\partial\bar{S}/\partial\ell$ of eigenstates from the middle of the spectrum ($\epsilon = 0.5$) of *one disorder realization* with $\ell = L/4$. For each value of the disorder strength h , the distribution is sampled from ≈ 1000 disorder realizations. Black curves indicate the mean of the distribution. Red dashed lines mark the largest standard deviations of the mean curves. A comparison of the results for system sizes $L = 20$ and $L = 12$ shows that for larger systems the states close to the critical point of *one disorder realization* become more diverse.

span a wider range of standard deviations as the system size grows. There are therefore disorder realizations for which there is essentially no variance and disorder realizations for which there is large variance among the eigenstates. This is the opposite of what we would expect if these eigenstates were independent, implying significant correlation between them. Secondly, both the average per-sample standard deviation is larger and the plurality of samples lie at higher standard deviations. This can be seen in Fig. 9 where the red dashed lines correspond to the means of the distributions at their maxima. Note that the maximum of the distribution is actually larger than the mean close to the MBL transition, showing that typical realizations exhibit a mix of volume and area law states (increasingly diverse for larger systems).

If these trends continue this means that the bimodality of the SCAEE distribution would arise at a single disorder realization level, and become more and more common for increasing system sizes. To verify that bimodality is present for single disorder realizations, we numerically analyzed 500 disorder realizations of system size $L = 16$ and a disorder strength $h = 2.69$ that corresponds to the variance peak location of the SCAEE at $\ell/L = 1/4$. Each sample has about 6000 eigenstates within the energy density window of $[0.45, 0.55]$. Among the 500 samples, the

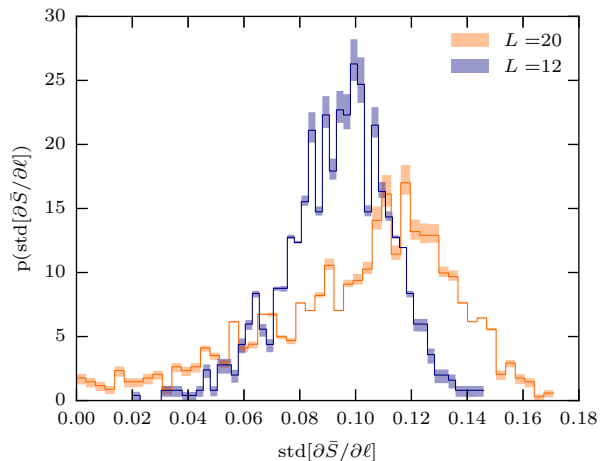


Figure 10. Histograms of horizontal slices ($h = 2.6$ for $L = 12$ and $h = 2.8$ for $L = 20$) through the mean curves' largest standard deviation points of Fig. 9. In comparison, the one disorder realization distribution for a larger system size has more weight shifted towards higher standard deviation, which indicates a higher likelihood of finding bimodality in a single sample.

one with the largest standard deviation is shown in Fig. 11. The distribution of the SCAEE for this sample is strikingly bimodal. Note that this is not a result of the curvature of the mobility edge, because the distribution of the SCAEE has no visible dependence on energy density as seen in the inset of Fig. 11. Especially, for this sample, the distributions of the SCAEE of the eigenstates within energy density windows of $[0.45, 0.50]$, $[0.50, 0.55]$, and $[0.45, 0.475] \cup [0.525, 0.55]$ are all bimodal and very similar to each other. Therefore, bimodality does indeed seem to be a generic feature of the SCAEE of individual disorder realizations.

We speculate that the mechanism for this bimodality may be caused by a mix of quasi-local and extended τ operators^{17,18,55} at the transition, where volume law states correspond to corresponding occupied extended orbitals and area law states are given by an occupation of only localized orbitals.

B. Correlations between the entanglement entropy and its derivatives

In this section we show the nearly complete correlation between the CAEE density \bar{S}/L and the SCAEE $\partial\bar{S}/\partial\ell$ and between $\partial\bar{S}/\partial\ell$ and $\partial^2\bar{S}/\partial\ell^2$ at a fixed subsystem ratio ℓ/L (which we choose as $1/4$), for various system sizes. These correlations are particularly compelling in the transition region, where, for finite system sizes, all accessible entropy densities are present (due to the wide and even bimodal distributions, depending on system size). This suggests that in the approach to the TDL there is a universal one-parameter family of curves

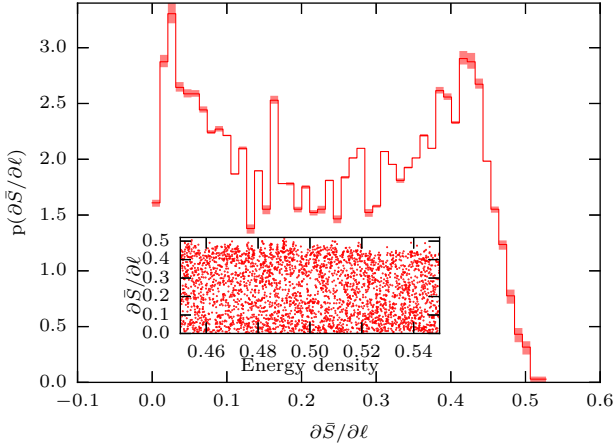


Figure 11. SCAEE distribution of a single disorder realization that has the largest standard deviation among the 500 samples at $L = 16$. Each sample contains 6000 eigenstates, with disorder strength h corresponding to the variance peak location of SCAEE evaluated at $\ell/L = 1/4$ as in Fig. 4. The inset shows SCAEE vs. energy density of each eigenstate of this disorder sample. Bimodality is clearly visible, and not likely due to the curvature of mobility edge.

\bar{S}/L in the transition region parameterized by (for example) the value of the \bar{S}/L at any fixed ℓ/L .

1. Correlation between \bar{S}/L and $\partial\bar{S}/\partial\ell$

We show two dimensional histograms of \bar{S}/L vs. $\partial\bar{S}/\partial\ell$ at various disorder strengths in Fig. 12 for systems of size $L = 20$, together with the mean curves for $L = 12, 16, 20$ on the same plot. The color scale is logarithmic in the probability density.

The red lines are upper and lower bounds of \bar{S}/L as a function of $\partial\bar{S}/\partial\ell$, that can be derived from the SSA constraints: Because of the SSA constraint and the fact that the slope is bounded from above by $\ln 2$, we have

$$\int_0^{L/4} \frac{\partial\bar{S}(L/4)}{\partial\ell} d\ell \leq \int_0^{L/4} \frac{\partial\bar{S}(\ell)}{\partial\ell} d\ell \leq \int_0^{L/4} \ln 2 d\ell \quad (11)$$

which reduces to

$$\frac{1}{4} \frac{\partial\bar{S}(L/4)}{\partial\ell} \leq \frac{\bar{S}(L/4)}{L} \leq \frac{\ln 2}{4} \quad (12)$$

At small disorder strength ($h = 2.0$), substantial weight is centered around $\partial\bar{S}/\partial\ell = \ln 2$ and $\bar{S}/L = \ln(2)/4$, indicating volume law entanglement. A light tail extending all the way to the MBL (low entanglement and low slope) region is visible.

At large disorder strength ($h = 4.8$), the weight is primarily around $\partial\bar{S}/\partial\ell = 0$ and $\bar{S}/L = 0$, indicating area law entanglement. Again, a light tail extends to the ergodic region. At intermediate disorder strengths, for

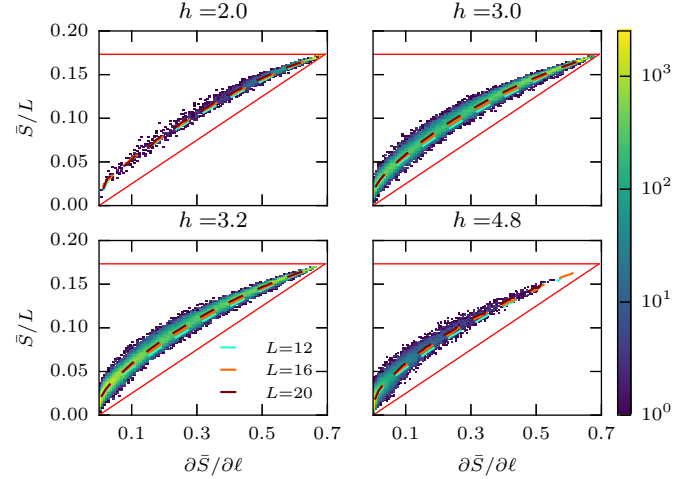


Figure 12. Two dimensional histogram of CAEE vs. SCAEE for systems of size $L = 20$ and $\ell = L/4$, at disorder strength $h = 2.0, 3.0, 3.2, 4.0$. The mean curves for $L = 12, 16$ are also shown in the figure. The color bar indicates the bin counts on a logarithmic scale. The red straight lines indicate the upper ($\bar{S}/L \leq \ln 2/4$) and lower ($\bar{S}/L \geq \frac{1}{4} \partial\bar{S}/\partial\ell$) bounds of the entanglement entropy. The mean curves are nearly converged, indicating possible universal behavior.

$L = 20$, the weight spans from the ergodic to the MBL side.

Notice, that there appears to be significant correlation between the CAEE and SCAEE and that the mean of these distributions seems to be largely independent of system size (at least from $L = 12$ to $L = 20$). In fact, even for different disorder distributions the banana-shaped histograms are located in the same region.

Besides, as discussed in Sec. B, we show that the width of the ‘banana’ becomes narrower and more centered around the mean values for larger system sizes.

All these points above are strongly suggesting the existence a one-parameter family of curves of \bar{S}/L in the transition region as a function of $\partial\bar{S}/\partial\ell$ in the approach to the TDL. We also observed that the weight in the middle of the ‘banana’ becomes diminished with increasing system sizes, consistent with the previously discussed bimodality.

2. Correlation between $\partial\bar{S}/\partial\ell$ and $L(\partial^2\bar{S}/\partial\ell^2)$

We also consider the correlations between $\partial\bar{S}/\partial\ell$ and $L(\partial^2\bar{S}/\partial\ell^2)$ again finding significant correlation between them. The two dimensional histograms of $\partial\bar{S}/\partial\ell$ vs. $L(\partial^2\bar{S}/\partial\ell^2)$ at various disorder strengths are shown in Fig. 13 for systems of size $L = 20$, together with the mean curves for $L = 12, 16, 20$ on the same plot.

Similarly, one can make the following observations. At small disorder strength, the distribution is centered around $\partial\bar{S}/\partial\ell = \ln 2$ and $L(\partial^2\bar{S}/\partial\ell^2) = 0$, indicat-

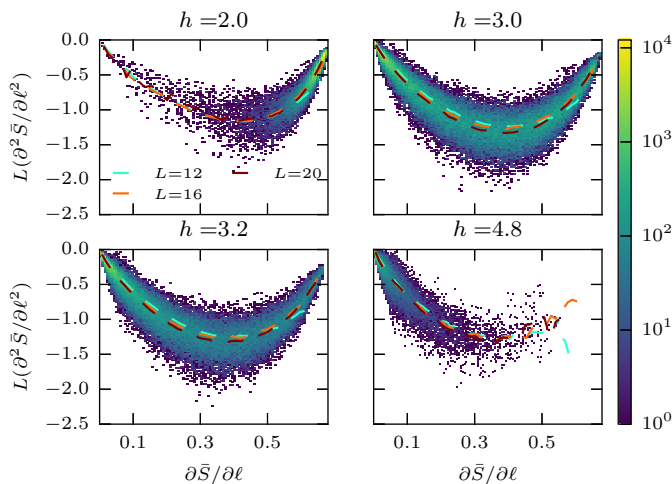


Figure 13. Two dimensional histogram of 2nd order derivative of CAEE vs. SCAEE for systems of size $L = 20$ and $\ell = L/4$, at $h = 2.0, 3.0, 3.2, 4.0$. The mean curves for $L = 12, 16$ are also shown on the graphs. The color bar indicates the bin counts at a log scale. The mean curves are nearly converged, indicating possible universal behavior.

ing volume law entanglement entropy. At large disorder strength, the distribution is centered around $\partial\bar{S}/\partial\ell = 0$ and $L(\partial^2\bar{S}/\partial\ell^2) = 0$, indicating area law entanglement. At intermediate disorder strengths, the weights of the histograms span the high entanglement and low entanglement regions. In addition, the lack of weight with concavity zero at values distant from zero or $\ln(2)$ slope indicates that we never see volume law (strictly linear) curves with non-thermal (non- $\ln(2)$) or non-zero slope. Again, we find that curves of system sizes between $L = 12$ and $L = 20$ have nearly identical means, and the width of the ‘U’ shaped distribution becomes narrower and more centered around the mean values for larger system sizes, as discussed in Sec. B.

V. CONCLUSION

We have presented an analysis of the scaling of the entanglement entropy up to the largest accessible system sizes in state of the art exact diagonalization and introduced the cut averaged entanglement entropy (CAEE) as well as its derivatives (SCAEE, *etc.*) with respect to subsystem size ℓ in periodic chains. We anticipate that the CAEE and SCAEE will be useful quantities to study the scaling behavior of the entanglement entropy of *single eigenstates* in other inhomogeneous systems.

We find that the slope of the cut averaged entanglement entropy (SCAEE) reproduces perfectly the volume law to area law transition associated with the MBL transition. We have also studied the slope without performing the cut average and observe increasing weight at negative slopes, which we argue to be associated with rare

localized regions, which appear already in the ergodic phase and are believed to be responsible for subdiffusion.

More interestingly, the probability distribution of the cut averaged entanglement entropy slope becomes sharply bimodal for large system sizes in the transition region, leading to eigenstates which have near zero and near maximal slope. The variance of this distribution in the critical regime grows with system size, already exceeding the largest variance possible for a unimodal distribution at $L = 20$. In addition, we find that the scaling of the CAEE is mostly linear in subsystem size at the variance peak with either maximal ($\ln 2$) or minimal (0) slope, but no state displays an intermediate value of the SCAEE and zero curvature. At the variance peak this implies that the scaling of the disorder averaged entanglement entropy is a volume law with a coefficient below its thermal value. We want to emphasize that due to the bimodal distribution, almost no state will show this behavior.

An extrapolation of the current trend is not inconsistent with the scenario that the variance peak would reach the largest possible variance in the TDL, which would lead to a coefficient of the volume law at half the thermal value of $\ln(2)$ (in the disorder average).

An important finding of our work is that this mixture of states is intrinsic and occurs in single disorder realizations. Interestingly enough, it seems that there is significant correlation between eigenstates in a disorder realization and some such realizations actually have essentially no variance in their SCAEE of states within a tiny energy window. This mixture of states is potentially connected to the important open question on the nature of the local integrals of motion at the transition. In addition, at the system sizes we can access, we see a clear distinction between the standard deviations of SCAEE of the inter and intra disordered samples (comparing bottom panel of Fig. 4 and black curves of Fig. 9). If this difference survives to the TDL, this suggests a breakdown of self averaging

In the final part of this paper, we discussed the correlation between the cut averaged entanglement entropy slope and the entropy itself and find that for large systems the value of the slope is a strong predictor of the value of the entropy suggesting a one-parameter family of curves for the CAEE in the critical region in the approach to TDL. In particular, this observation allows us to draw conclusions on the behavior of the cut averaged entanglement entropy itself, which has to become bimodal, just as its slope.

On a more speculative note, the observed bimodal features of the distributions could be connected to the strong fluctuations of the entanglement entropy at the critical point in RG calculations^{27,56} and possibly to multifractal features²⁹.

ACKNOWLEDGMENTS

DJL is very grateful to F. Alet, N. Laflorencie and Y. Bar Lev for many inspiring discussions and fruitful collaborations. BKC acknowledges helpful discussions with Anushya Chandran, Shivaji Sondhi, David Huse, Vedika Kehmani, and David Pekker. We thank F. Alet, Y. Bar Lev, D. Huse, N. Laflorencie, V. Khemani and C. Monthus for their helpful comments on the manuscript. A significant part of the results presented here has been obtained using computational resources of CALMIP (grant 2015-P0677) and the LPT at Université Paul Sabatier at Toulouse, France.

This work was supported in part by the Gordon and Betty Moore Foundation's EPiQS Initiative through Grant No. GBMF4305 at the University of Illinois and the French ANR program ANR-11-IS04-005-01. Our code is partly based on the PETSc⁵⁷⁻⁵⁹, SLEPc⁶⁰ and MUMPS^{61,62} libraries.

This research is part of the Blue Waters sustained-petascale computing project, which is supported by the National Science Foundation (awards OCI-0725070 and ACI-1238993) and the State of Illinois. Blue Waters is a joint effort of the University of Illinois at Urbana-Champaign and its National Center for Supercomputing Applications.

BKC and XY acknowledge support from DOE, grant SciDAC FG02-12ER46875.

Appendix A: Lattice version of SSA constraint

On a lattice, the continuum formulation of Sec. II may seem artificial, however a completely analogous derivation can be obtained. In this scenario, the x and ϵ in Eq. (3) and Eq. (7) are integers (assuming lattice constant is 1). For the following discussion, we set $\epsilon = 1$.

Summing over all x on a periodic lattice for Eq. (3) and Eq. (7), one easily obtains

$$2\bar{S}(\ell) \geq \bar{S}(\ell+1) + \bar{S}(\ell-1), \quad (\text{A1})$$

and

$$2\bar{S}(\ell+1) \geq 2\bar{S}(\ell), \quad \ell < L/2. \quad (\text{A2})$$

Usually, one defines first and second order discrete derivatives with respect to ℓ as follows.

$$\Delta^+ \bar{S}(\ell) \equiv \bar{S}(\ell+1) - \bar{S}(\ell). \quad (\text{A3})$$

$$\Delta \bar{S}(\ell) \equiv \frac{\bar{S}(\ell+1) - \bar{S}(\ell-1)}{2}. \quad (\text{A4})$$

$$\Delta^- \bar{S}(\ell) \equiv \bar{S}(\ell) - \bar{S}(\ell-1). \quad (\text{A5})$$

$$\Delta^2 \bar{S}(\ell) \equiv \bar{S}(\ell+1) + \bar{S}(\ell-1) - 2\bar{S}(\ell). \quad (\text{A6})$$

Then we have the following SSA constraints concerning the discrete derivatives.

$$\Delta^2 \bar{S}(\ell) \leq 0. \quad (\text{A7})$$

$$\Delta^+ \bar{S}(\ell) \geq 0, \quad \Delta \bar{S}(\ell) \geq 0, \quad \Delta^- \bar{S}(\ell) \geq 0, \quad \ell < L/2. \quad (\text{A8})$$

In the present work, however, we use the continuum version of the SSA constraints by an analytic continuation of the $\bar{S}(\ell)$ curve, because it allows us to study incommensurate subsystem sizes. This is important due to the serious constraints in available system sizes from exact diagonalization.

Appendix B: Standard deviations of the correlations distributions

In Section IV B, we discussed the correlations between the CAEE density \bar{S}/L and the SCAEE $\partial \bar{S}/\partial \ell$ and between $\partial \bar{S}/\partial \ell$ and $\partial^2 \bar{S}/\partial \ell^2$ at a fixed subsystem ratio ℓ/L (which we choose as $1/4$), as shown in Fig 12 and 13. Here we further examine these distributions to establish the standard deviation, or spread, of each distribution around its mean, finding it narrower as the system size grows.

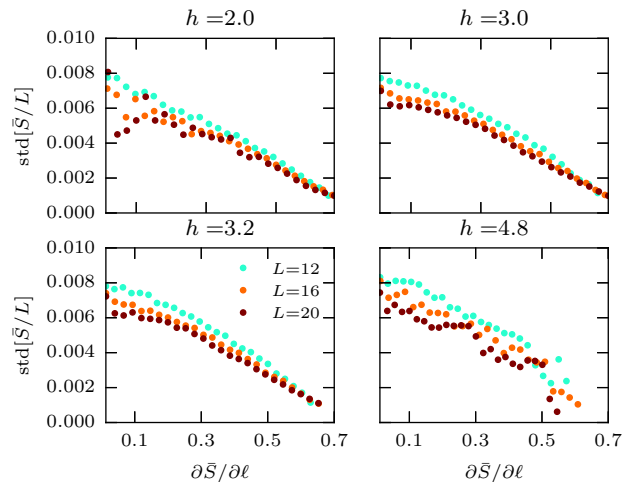


Figure 14. Standard deviation of vertical slices of CAEE vs. SCAEE histograms as in Fig. 12, for systems of size $L = 20$ and $\ell = L/4$, at $h = 2.0, 3.0, 3.2, 4.0$. The standard deviations decrease with system size. The 3rd and the 4th cumulants (not included) of the vertical slices of the histograms shows that the vertical distributions become more Gaussian with increasing system size.

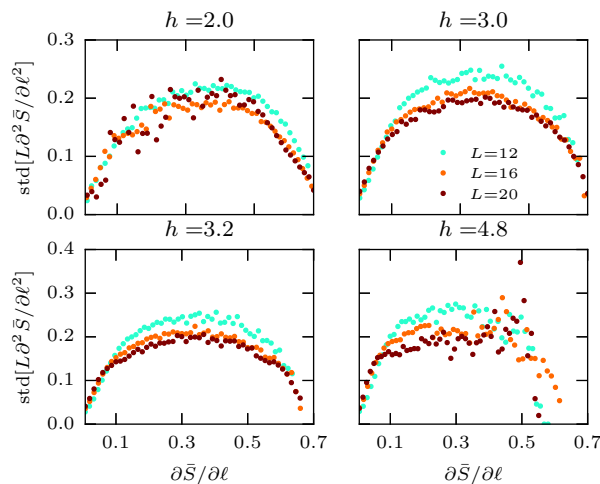


Figure 15. Standard deviation of vertical slices of 2nd order derivative of CAEE vs. SCAEE histograms as in Fig. 13, for systems of size $L = 20$ and $\ell = L/4$, at $h = 2.0, 3.0, 3.2, 4.0$. The standard deviations decreases with system size. The 3rd and the 4th cumulants (not included) of the vertical slices of the histograms shows that the vertical distributions become more Gaussian with increasing system size.

For the 2D histograms of the CAEE density \bar{S}/L and the SCAEE $\partial\bar{S}/\partial\ell$, we consider a slice of the two dimensional histograms vertically around a fixed value of $\partial\bar{S}/\partial\ell$. This vertical slice gives a distribution of different \bar{S}/L values at some fixed value of $\partial\bar{S}/\partial\ell$. We calculated the third and fourth cumulants of these distributions, and find their absolute values to be less than 10^{-6} for $L = 12$ and even smaller for larger L ; therefore these vertical slices are very likely Gaussian with well behaved mean and variances. The standard deviations of these vertical slices are shown in Fig. 14, which exhibit a slow decrease with system size. Similarly, for the 2D histograms of the $\partial\bar{S}/\partial\ell$ and $L\partial^2\bar{S}/\partial\ell^2$, we also looked at the distribution of vertical slices of the two dimensional histograms. The standard deviations of these vertical slices are shown in Fig. 15, which exhibits a slow decrease with system size. Calculating the third and fourth cumulants also suggests that these distributions become more and more Gaussian with increasing system sizes.

- ¹ D. M. Basko, I. L. Aleiner, and B. L. Altshuler, “Metal-insulator transition in a weakly interacting many-electron system with localized single-particle states,” *Annals of Physics* **321**, 1126–1205 (2006).
- ² I. V. Gornyi, A. D. Mirlin, and D. G. Polyakov, “Interacting Electrons in Disordered Wires: Anderson Localization and Low-T Transport,” *Phys. Rev. Lett.* **95**, 206603 (2005).
- ³ P. W. Anderson, “Absence of Diffusion in Certain Random Lattices,” *Phys. Rev.* **109**, 1492–1505 (1958).
- ⁴ J. M. Deutsch, “Quantum statistical mechanics in a closed system,” *Phys. Rev. A* **43**, 2046–2049 (1991).
- ⁵ Mark Srednicki, “Chaos and quantum thermalization,” *Phys. Rev. E* **50**, 888–901 (1994).
- ⁶ Marcos Rigol, Vanja Dunjko, and Maxim Olshanii, “Thermalization and its mechanism for generic isolated quantum systems,” *Nature* **452**, 854–858 (2008).
- ⁷ Luca D’Alessio, Yariv Kafri, Anatoli Polkovnikov, and Marcos Rigol, “From Quantum Chaos and Eigenstate Thermalization to Statistical Mechanics and Thermodynamics,” *arXiv:1509.06411 [cond-mat, physics:quant-ph]* (2015), *arXiv: 1509.06411*.
- ⁸ Gilles Montambaux, Didier Poilblanc, Jean Bellissard, and Clément Sire, “Quantum chaos in spin-fermion models,” *Phys. Rev. Lett.* **70**, 497–500 (1993).
- ⁹ Ph. Jacquod and D. L. Shepelyansky, “Emergence of Quantum Chaos in Finite Interacting Fermi Systems,” *Phys. Rev. Lett.* **79**, 1837–1840 (1997).
- ¹⁰ B. Georgeot and D. L. Shepelyansky, “Integrability and Quantum Chaos in Spin Glass Shards,” *Phys. Rev. Lett.* **81**, 5129–5132 (1998).
- ¹¹ Pil Hun Song and Dima L. Shepelyansky, “Low-energy transition in spectral statistics of two-dimensional inter-

- acting fermions,” *Phys. Rev. B* **61**, 15546–15549 (2000).
- ¹² Vadim Oganesyan and David A. Huse, “Localization of interacting fermions at high temperature,” *Phys. Rev. B* **75**, 155111 (2007).
- ¹³ Arijeet Pal and David A. Huse, “Many-body localization phase transition,” *Phys. Rev. B* **82**, 174411 (2010).
- ¹⁴ David J. Luitz, Nicolas Laflorencie, and Fabien Alet, “Many-body localization edge in the random-field Heisenberg chain,” *Phys. Rev. B* **91**, 081103 (2015).
- ¹⁵ Maksym Serbyn and Joel E. Moore, “Spectral statistics across the many-body localization transition,” *Phys. Rev. B* **93**, 041424 (2016).
- ¹⁶ Cecile Monthus, “Level repulsion exponent beta for Many-Body Localization Transitions and for Anderson Localization Transitions via Dyson Brownian Motion,” *Journal of Statistical Mechanics: Theory and Experiment* **2016**, 033113 (2016), *arXiv: 1510.08322*.
- ¹⁷ Maksym Serbyn, Z. Papić, and Dmitry A. Abanin, “Local Conservation Laws and the Structure of the Many-Body Localized States,” *Phys. Rev. Lett.* **111**, 127201 (2013).
- ¹⁸ John Z. Imbrie, “On Many-Body Localization for Quantum Spin Chains,” *arXiv:1403.7837 [cond-mat, physics:math-ph]* (2014), *arXiv: 1403.7837*.
- ¹⁹ David A. Huse, Rahul Nandkishore, and Vadim Oganesyan, “Phenomenology of fully many-body-localized systems,” *Phys. Rev. B* **90**, 174202 (2014).
- ²⁰ Bela Bauer and Chetan Nayak, “Area laws in a many-body localized state and its implications for topological order,” *J. Stat. Mech.* **2013**, P09005 (2013).
- ²¹ David J. Luitz, “Long tail distributions near the many-body localization transition,” *Phys. Rev. B* **93**, 134201 (2016).
- ²² Xiongjie Yu, David Pekker, and Bryan K. Clark,

- “Finding matrix product state representations of highly-excited eigenstates of many-body localized Hamiltonians,” [arXiv:1509.01244 \[cond-mat\]](#) (2015), [arXiv: 1509.01244](#).
- ²³ Vedika Khemani, Frank Pollmann, and S. L. Sondhi, “Obtaining highly-excited eigenstates of many-body localized Hamiltonians by the density matrix renormalization group,” [arXiv:1509.00483 \[cond-mat\]](#) (2015), [arXiv: 1509.00483](#).
 - ²⁴ S. P. Lim and D. N. Sheng, “Nature of Many-Body Localization and Transitions by Density Matrix Renormalization Group and Exact Diagonalization Studies,” [arXiv:1510.08145 \[cond-mat\]](#) (2015), [arXiv: 1510.08145](#).
 - ²⁵ James R. Garrison and Tarun Grover, “Does a single eigenstate encode the full Hamiltonian?” [arXiv:1503.00729 \[cond-mat, physics:hep-th, physics:quant-ph\]](#) (2015), [arXiv: 1503.00729](#).
 - ²⁶ Tarun Grover, “Certain General Constraints on the Many-Body Localization Transition,” [arXiv:1405.1471 \[cond-mat, physics:quant-ph\]](#) (2014), [arXiv: 1405.1471](#).
 - ²⁷ Ronen Vosk, David A. Huse, and Ehud Altman, “Theory of the Many-Body Localization Transition in One-Dimensional Systems,” *Phys. Rev. X* **5**, 031032 (2015).
 - ²⁸ Scott D. Geraedts, Rahul Nandkishore, and Nicolas Regnault, “Many-body localization and thermalization: Insights from the entanglement spectrum,” *Phys. Rev. B* **93**, 174202 (2016).
 - ²⁹ Cecile Monthus, “Many-Body-Localization Transition : strong multifractality spectrum for matrix elements of local operators,” [arXiv:1603.04701 \[cond-mat\]](#) (2016), [arXiv: 1603.04701](#).
 - ³⁰ Cecile Monthus, “Many Body Localization Transition in the strong disorder limit : entanglement entropy from the statistics of rare extensive resonances,” *Entropy* **18**, 122 (2016), [arXiv: 1510.03711](#).
 - ³¹ David J. Luitz and Yevgeny Bar Lev, “Anomalous thermalization in ergodic systems,” [arXiv:1607.01012 \[cond-mat\]](#) (2016), [arXiv: 1607.01012](#).
 - ³² With Rényi index 1.
 - ³³ Elliott H. Lieb and Mary Beth Ruskai, “Proof of the strong subadditivity of quantum-mechanical entropy,” *Journal of Mathematical Physics* **14**, 1938–1941 (1973).
 - ³⁴ Elliott H. Lieb, “Some convexity and subadditivity properties of entropy,” *Bulletin of the American Mathematical Society* **81**, 1–13 (1975).
 - ³⁵ Göran Lindblad, “Completely positive maps and entropy inequalities,” *Communications in Mathematical Physics* **40**, 147–151 (1975).
 - ³⁶ Mary Beth Ruskai, “Inequalities for quantum entropy: A review with conditions for equality,” *Journal of Mathematical Physics* **43**, 4358–4375 (2002).
 - ³⁷ Marko Žnidarič, Tomaž Prosen, and Peter Prelovšek, “Many-body localization in the Heisenberg XXZ magnet in a random field,” *Phys. Rev. B* **77**, 064426 (2008).
 - ³⁸ A. De Luca and A. Scardicchio, “Ergodicity breaking in a model showing many-body localization,” *EPL* **101**, 37003 (2013).
 - ³⁹ David Pekker and Bryan K. Clark, “Encoding the structure of many-body localization with matrix product operators,” [arXiv:1410.2224 \[cond-mat\]](#) (2014), [arXiv: 1410.2224](#).
 - ⁴⁰ Maksym Serbyn, Z. Papić, and Dmitry A. Abanin, “Criterion for Many-Body Localization-Delocalization Phase Transition,” *Phys. Rev. X* **5**, 041047 (2015).
 - ⁴¹ Soumya Bera, Henning Schomerus, Fabian Heidrich-Meisner, and Jens H. Bardarson, “Many-Body Localization Characterized from a One-Particle Perspective,” *Phys. Rev. Lett.* **115**, 046603 (2015).
 - ⁴² David J. Luitz, Nicolas Laflorencie, and Fabien Alet, “Extended slow dynamical regime close to the many-body localization transition,” *Phys. Rev. B* **93**, 060201 (2016).
 - ⁴³ Rajeev Singh, Jens H. Bardarson, and Frank Pollmann, “Signatures of the many-body localization transition in the dynamics of entanglement and bipartite fluctuations,” *New J. Phys.* **18**, 023046 (2016).
 - ⁴⁴ Frank Pollmann, Vedika Khemani, J. Ignacio Cirac, and S. L. Sondhi, “Efficient variational diagonalization of fully many-body localized Hamiltonians,” [arXiv:1506.07179 \[cond-mat\]](#) (2015), [arXiv: 1506.07179](#).
 - ⁴⁵ Soumya Bera and Arul Lakshminarayanan, “Local entanglement structure across a many-body localization transition,” *Phys. Rev. B* **93**, 134204 (2016).
 - ⁴⁶ Trithip Devakul and Rajiv R. P. Singh, “Early Breakdown of Area-Law Entanglement at the Many-Body Delocalization Transition,” *Phys. Rev. Lett.* **115**, 187201 (2015).
 - ⁴⁷ Jonas A. Kjäll, Jens H. Bardarson, and Frank Pollmann, “Many-Body Localization in a Disordered Quantum Ising Chain,” *Phys. Rev. Lett.* **113**, 107204 (2014).
 - ⁴⁸ Xiao Chen, Xiongjie Yu, Gil Young Cho, Bryan K. Clark, and Eduardo Fradkin, “Many-body localization transition in Rokhsar-Kivelson-type wave functions,” *Phys. Rev. B* **92**, 214204 (2015).
 - ⁴⁹ We have tried a tentative extrapolation of the peak height to the thermodynamic limit using a polynomial ansatz as a function of $1/L$, pointing to a maximal variance of $\ln 2/2$, although this extrapolation is not reliable, as the extrapolation typically overshoots the theoretical maximum due to finite size effects.
 - ⁵⁰ Andrew C. Potter, Romain Vasseur, and S. A. Parameswaran, “Universal Properties of Many-Body Delocalization Transitions,” *Phys. Rev. X* **5**, 031033 (2015).
 - ⁵¹ Yevgeny Bar Lev, Guy Cohen, and David R. Reichman, “Absence of Diffusion in an Interacting System of Spinless Fermions on a One-Dimensional Disordered Lattice,” *Phys. Rev. Lett.* **114**, 100601 (2015).
 - ⁵² Kartiek Agarwal, Sarang Gopalakrishnan, Michael Knap, Markus Müller, and Eugene Demler, “Anomalous Diffusion and Griffiths Effects Near the Many-Body Localization Transition,” *Phys. Rev. Lett.* **114**, 160401 (2015).
 - ⁵³ Vipin Kerala Varma, Alessio Leroche, Francesca Pietracaprina, John Goold, and Antonello Scardicchio, “Energy diffusion in the ergodic phase of a many body localizable spin chain,” [arXiv:1511.09144 \[cond-mat, physics:quant-ph\]](#) (2015), [arXiv: 1511.09144](#).
 - ⁵⁴ Sarang Gopalakrishnan, Kartiek Agarwal, Eugene A. Demler, David A. Huse, and Michael Knap, “Griffiths effects and slow dynamics in nearly many-body localized systems,” *Phys. Rev. B* **93**, 134206 (2016).
 - ⁵⁵ Sarang Gopalakrishnan and Rahul Nandkishore, “Mean-field theory of nearly many-body localized metals,” *Phys. Rev. B* **90**, 224203 (2014).
 - ⁵⁶ David Pekker, Gil Refael, Ehud Altman, Eugene Demler, and Vadim Oganesyan, “Hilbert-Glass Transition: New Universality of Temperature-Tuned Many-Body Dynamical Quantum Criticality,” *Phys. Rev. X* **4**, 011052 (2014).
 - ⁵⁷ Satish Balay, Shrirang Abhyankar, Mark F. Adams, Jed Brown, Peter Brune, Kris Buschelman, Victor Eijkhout, William D. Gropp, Dinesh Kaushik, Matthew G. Knepley, Lois Curfman McInnes, Karl Rupp, Barry F. Smith, and Hong Zhang, “PETSc Web page,” <http://www.mcs.anl>.

- [gov/petsc](http://www.solveradvice.org/petsc) (2014).
- ⁵⁸ Satish Balay, Shrirang Abhyankar, Mark F. Adams, Jed Brown, Peter Brune, Kris Buschelman, Victor Eijkhout, William D. Gropp, Dinesh Kaushik, Matthew G. Knepley, Lois Curfman McInnes, Karl Rupp, Barry F. Smith, and Hong Zhang, *PETSc Users Manual*, Tech. Rep. ANL-95/11 - Revision 3.5 (Argonne National Laboratory, 2014).
- ⁵⁹ Satish Balay, William D. Gropp, Lois Curfman McInnes, and Barry F. Smith, “Efficient management of parallelism in object oriented numerical software libraries,” in *Modern Software Tools in Scientific Computing*, edited by E. Arge, A. M. Bruaset, and H. P. Langtangen (Birkhäuser Press, 1997) pp. 163–202.
- ⁶⁰ Vicente Hernandez, Jose E. Roman, and Vicente Vidal, “SLEPc: A Scalable and Flexible Toolkit for the Solution of Eigenvalue Problems,” *ACM Trans. Math. Softw.* **31**, 351–362 (2005).
- ⁶¹ P. R. Amestoy, I. S. Duff, J. Koster, and J.-Y. L’Excellent, “A fully asynchronous multifrontal solver using distributed dynamic scheduling,” *SIAM J. Matrix Anal. Appl.* **23**, 15–41 (2001).
- ⁶² P. R. Amestoy, A. Guermouche, J.-Y. L’Excellent, and S. Pralet, “Hybrid scheduling for the parallel solution of linear systems,” *Parallel Computing* **32**, 136–156 (2006).